Exploring a lower resolution physics grid in CAM-SE-CSLAM

A.R. Herrington[1]*, P.H. Lauritzen[2], S. Goldhaber[2], Mark A. Taylor[3], K.A. Reed[1]

[1]School of Marine and Atmospheric Sciences, Stony Brook University, Stony Brook, New York
[2]National Center for Atmospheric Research, Boulder, Colorado, USA
[3]Sandia National Laboratories, Albuquerque, New Mexico, USA

Key Points:

-
-
-

*Stony Brook, New York

Corresponding author: Adam R. Herrington, `adam.herrington@stonybrook.edu`

Abstract

1 Introduction

Global atmospheric models fundamentally consist of two components. The dynamical core (*dynamics*), which numerically integrate the adiabatic equations of motion and tracer advection, and the physical parameterizations (*physics*), which compute the effects of diabatic and subgrid-scale processes (e.g., radiative transfer and moist convection) on the grid-scale. More out of convenience than anything else, the physics are evaluated on the dynamics grid, i.e., the physics grid and dynamics grid coincide. From linear stability and accuracy analysis of numerical methods, it is a common result that the shortest simulated wavelengths are not accurately represented by the dynamical core. Additionally, simulated downscale cascades result in an unrealistic collection of energy and/or enstrophy near the truncation scale, which may be observed from kinetic energy spectra in model simulations [*Skamarock*, 2011]. Some form of dissipation must be incorporated into models to mitigate these numerical artifacts near the grid scale [*Jablonowski and Williamson*, 2011]. This numerical dissipation has no physical analogy [although see *Grinstein et al.*, 2007], and the grid-scale is therefore contaminated by numerous un-physical processes. The under-resolved nature of the grid-scale led *Lander and Hoskins* [1997] to speculate whether the physics should be evaluated on a grid that is more reflective of the scales actually resolved by the dynamical core.

Experimentation with different physics grid resolutions have so far been limited to models employing the spectral transform method [*Lander and Hoskins*, 1997; *Williamson*, 1999; *Wedi*, 2014]. *Lander and Hoskins* [1997] argue that passing under-resolved states to the physics may be especially problematic in spectral transform models, since the physics are evaluated on a latitude-longitude transform grid, and contains more degrees of freedom than the spectral representation to prevent aliasing of quadratic quantities. However, *Lander and Hoskins* [1997] indicate that the spectral truncation of the physics tendencies damps errors that may result from passing an under-resolved state to the physics, although the extent to which these errors may still be present in the model was not addressed.

Another class of spectral-transform models evaluate the quadratic terms using semi-Lagrangian methods, which are implicitly diffusive, relaxing constraints on the resolution of the transform grid. *Wedi* [2014] experimented with different transform grid resolutions and concluded that the standard high resolution quadratic grid actually improves forecast skill over the use of a lower-resolution transform grid. They suggests that increasing the resolution of the transform grid simulates a kind of sub-grid variability on the spectral state, which is thought to be under-represented in global atmospheric models [*Shutts*, 2005]. This is in principle the purpose of "super-parameterization," in which a cloud resolving model is embedded in each grid cell to simulate the requisite subgrid variability, and improves both diurnal and sub-seasonal variability in the model [*Randall et al.*, 2003].

After the physics tendencies are transformed into spectral space, the tendencies may be truncated at any particular wave number. *Williamson* [1999] conducted a pair of convergence tests using a global spectral transform model; a conventional convergence test and one in which the spectral truncation of the physics tendencies is held fixed and the resolution of the dynamical core increased. In contrast to the realistic weather forecasts of *Wedi* [2014], *Williamson* [1999] run their model to equilibrium in an idealized climate configuration. When the physics and dynamics resolutions increase together, as in more typical convergence studies, the strength of the Hadley Cell increases monotonically with resolution. This sensitivity of Hadley Cell strength to horizontal resolution is a common result of global models at hydrostatic resolutions [see *Herrington and Reed*, 2017, and references therein]. But with the truncation wave number of physics tendencies held fixed, the Hadley Cell showed very little sensitivity to dynamical core resolution, resembling the solution for which the dynamics truncation wave number is equal to that of the lower

resolution physics. *Herrington and Reed* [2017] speculate that the results of *Williamson* [1999] indicate that the scales of motion resolved by the dynamical core are aliased to the lower resolution physics. The results of *Williamson* [1999]; *Wedi* [2014] do not provide evidence that a lower resolution physics grid reduces computational errors in spectral transform models, but this was seldom discussed in either study.

Global spectral transform models, while remarkably efficient at small processor counts, do not scale well on massively parallel systems. High-order Galerkin methods are becoming increasingly popular in climate and weather applications due to their high-parallel efficiency, high-processor efficiency, high-order accuracy (for smooth problems), and geometric flexibility facilitating mesh-refinement applications. High resolution climate simulations with NCAR's Community Atmosphere Model [CAM; *Neale et al.*, 2012] are typically performed using a continuous Galerkin dynamical core referred to as CAM-SE [CAM Spectral Elements; *Taylor et al.*, 2008; *Dennis et al.*, 2012; *Lauritzen et al.*, 2018]. CAM-SE may be optionally coupled to a conservative, semi-Lagrangian tracer advection scheme for accelerated multi-tracer transport [CAM-SE-CSLAM; *Lauritzen et al.*, 2017]. Tracer advection then evolves on an entirely separate, finite-volume grid which contains the same degrees of freedom as CAM-SE's quadrature node grid.

Element-based Galerkin methods are susceptible to grid-imprinting, and may need be considered when contemplating a particular physics grid [*Herrington et al.*, in revision, hereafter referred to as HL18]. Grid imprinting manifests at the element boundaries, since the global basis is least smooth (C^0; all derivatives are discontinuous) for quadrature nodes lying on the element boundaries, and the gradients (e.g., the pressure gradient) are systematically tighter producing local extremes. Through computing the physics tendencies at the nodal points, element boundary extrema is also observed in the physics tendencies.

HL18 has shown that through evaluating the physics on the finite-volume tracer advection grid in CAM-SE-CSLAM, element boundary noise is substantially reduced, although still problematic in regions of steep terrain, at low latitudes. Through integrating CAM-SE's basis functions over the control volumes of the finite-volume grid, element boundary extrema is additionally weighted by the C^∞ solutions (i.e., the basis representation is infinitely smooth and all derivatives are continuous) of the element interior, and the state is smoother. Additionally, in defining an area averaged state, the finite-volume physics grid is made consistent with assumptions inherent to the physics, and is more appropriate for coupling to other model components (e.g., the land model), which is typically performed using finite-volume based mapping algorithms.

The finite-volume grid of HL18 is found through dividing the elements of CAM-SE's gnomic cubed-sphere grid with equally spaced, equi-angular coordinate lines parallel to the element boundaries, such that there are 3×3 control volumes per element (hereafter referred to as $pg3$). While a 3×3 physics grid was chosen in order to have the same degrees of freedom as the dynamical core, the control volumes encompass a region of the element in which their proximity to the element boundaries are not equal. Therefore, not every control volume in an element has the same smoothness properties. This may be avoided through defining a physics grid in which the elements are instead divided into 2×2 control volumes (hereafter referred to as $pg2$). The control volumes of the $pg2$ grid all have the same proximity to the element boundaries, and should mitigate the element boundary noise that remains in the $pg3$ grid, and shown in HL18.

In this study, we test the hypothesis that the coarser, $pg2$ physics grid is effective at reducing spurious noise at element boundaries, particularly over regions of rough topography. In addition, the recent trend towards running models at ever higher resolutions is an almost prohibitive computational burden. As the physics makes up over half of the computational cost in CAM-SE [*Lauritzen et al.*, 2018], the improvement in computational performance using a coarser resolution physics grid is potentially significant. However, any advantages of using a coarser physics grid need be weighed against any potential re-

duction in simulation quality, e.g., possible aliasing of the resolved scales of motion by the coarser grid, as suggested by the results of *Williamson* [1999]. Section 2 describes the implementation of the $pg2$ grid into CAM-SE-CSLAM. Section 3 provides the results of a hierarchy of model configurations to identify any changes in grid imprinting, or in the overall solution, compared with the $pg3$ configuration. Section 4 provides a discussion of the results and conclusions.

2 Methods

Separating dynamics, tracer and physics grids introduces the added complexity of having to map the state from dynamics and tracer grids to the physics grid; and mapping physics tracer tendencies back to the tracer grid and physics tendencies needed by the dynamical core to the dynamics grid. The dynamics grid refers to the Gauss-Lobatto-Legendre (GLL) quadrature nodes by the spectral-element method to solve the momentum equations for the momentum vector (u, v), thermodynamics equation for temperature (T), continuity equation for dry air (M), and continuity equations for water vapor and condensates thermodynamically active [see, e.g., *Lauritzen et al.*, 2018, for details]. By tracer grid we refer to the $pg3$ grid on which CSLAM performs tracer transport of water vapor, condensates and other tracers. The GLL value for water vapor and condensates is overwritten by the CSLAM values every physics time-step so that the spectral-element advection of water species does not become decoupled from the the CSLAM advection of the same water species. Mapping velocity components, dry air mass and temperature from the GLL grid to the $pg2$ grid is done by using the internal degree 3 Lagrange basis functions in CAM-SE [as described in *Herrington et al.*, in revision, for pg3; exactly the same methods can be used for $pg2$].

As compared to the $pg3$ configuration, the extra complication of the $pg2$ setup is that tracer state needs to be mapped from the tracer grid to the physics grid and tracer tendencies need to the mapped from the physics grid to CSLAM grid. In order to describe the algorithm some notation needs to be introduced.

The mapping algorithm is applied to each element Ω (with spherical area $\Delta\Omega$) so without loss of generality consider one element. Let $\Delta A_k^{(pg)}$ and $\Delta A_\ell^{(nc)}$ be the spherical area of the physics grid grid cell $A_k^{(pg)}$ and CSLAM control volume $A_\ell^{(nc)}$, respectively. The physics grid cells and CSLAM cells respectively span the element without gaps or overlaps

$$\cup_{k=1}^{pg^2} A_k^{(pg)} = \Omega \text{ and } A_k^{(pg)} \cap A_\ell^{(pg)} = \emptyset \quad \forall k \neq \ell, \tag{1}$$

$$\cup_{k=1}^{nc^2} A_k^{(nc)} = \Omega \text{ and } A_k^{(nc)} \cap A_\ell^{(nc)} = \emptyset \quad \forall k \neq \ell. \tag{2}$$

The overlap areas between the k-th physics grid cell and CSLAM cells is denoted

$$A_{k\ell} = A_k^{(pg)} \cap A_\ell^{(nc)}, \tag{3}$$

so that

$$A_k^{(pg)} = \cup_{l=1}^{nc^2} A_{k\ell}. \tag{4}$$

This overlap grid is also referred to as an exhange grid.

2.1 Mapping tracers from CSLAM to pg

For mapping tracer state from the CSLAM grid to any physics grid can be done using exising CSLAM technology, i.e. do a high-order shape-preserving reconstruction of mixing ratio and dry air mass inside each CSLAM control volume and integrate those reconstruction functions over the overlap areas [**??**]. This algorithm retains the properties of CSLAM: inherent mass-conservation, mixing ratio shape-preservation and linear-correlation preservation.

In mathemtical terms the remapping is given by

$$\Delta M_\ell^{(pg)} \Delta A_\ell = \sum_{k=1}^{nc^2} \Delta M_{k\ell}^{(nc)} \Delta A_{k\ell}, \tag{5}$$

$$\Delta M_\ell^{(pg)} m_\ell^{(pg)} \Delta A_\ell = \frac{1}{\Delta M_\ell^{(pg)}} \sum_{k=1}^{nc^2} [\Delta M\, m]_{k\ell}^{(nc)} \Delta A_{k\ell}, \tag{6}$$

where

$$\Delta M_{k\ell}^{(nc)} = \frac{1}{\Delta A_{k\ell}} \int_{A_{k\ell}} \Delta M(x,y) dA. \tag{7}$$

$$[\Delta M\, m]_{k\ell}^{(nc)} = \frac{1}{\Delta A_{k\ell}} \int_{A_{k\ell}} [\Delta M\, m](x,y)\, dA. \tag{8}$$

The tendencies from the parameterizations are computed on the physics grid. The tracer tendency in physics grid cell k is denoted $f_k^{(pg)}$. The problem is how to map $f_k^{(pg)}$ to the CSLAM control volumes $f^{(nc)}$ satisfying the following constraints:

1. **Local mass-conservation**

$$f_k^{(pg)} \Delta p_k^{(pg)} = \cup_{\ell=1}^{nc^2} \Delta A_{k\ell} \Delta p_\ell^{(nc)} f_\ell^{(nc)}, \tag{9}$$

   where $\Delta p_k^{(pg)}$ is the pressure level thickness in physics grid cell k and similarly for $\Delta p^{(nc)}$.

2. **Shape-preservation in mixing ratio**: The forcing on the CSLAM grid should not produce a value smaller than the new physics grid mixing ratio, $m_k^{(pg)} + \Delta t f_k^{(pg)}$ or a value smaller than the existing CSLAM mixing ratios over the overlap areas $m_{k\ell}^{(nc)}$

$$m_k^{(min)} = \min\left(m_k^{(pg)} + \Delta t f_k^{(pg)}, \left\{ m_{k\ell}^{(nc)} | \ell = 1, nc^2 \right\}\right), \tag{10}$$

   where Δt is the physics time-step. Similarly for maxima

$$m_k^{(max)} = \max\left(m_k^{(pg)} + \Delta t f_k^{(pg)}, \left\{ m_{k\ell}^{(nc)} | \ell = 1, nc^2 \right\}\right), \tag{11}$$

3. **Linear correlation preservation**: The physics forcing must not disrupt linear tracer correlation between species on the CSLAM grid [see, e.g., *Lauritzen and Thuburn*, 2012].

4. **Consistency**: A constant mixing ratio tendency, *cnst*, on the physics grid, $f_k^{(pg)} = cnst\ \forall k$, must result in the same (constant) forcing on the CSLAM grid, $f_\ell^{(nc)} = f_k^{(pg)} = cnst\ \forall \ell$.

To motivate the algorithm that will simultaneously satisfy 1-4 it is informative to discuss how 'standard' mapping algorithms will violate one or more of the constraints.

- Conservative remapping:
- Interpolation:

some text about how challenging it is to satisfy 1-3 simultaneously

2.2 Algorithm

In the *pg*2 configuration, mapping the fields to and from the quadrature grid and *pg*2 grid is identical to that described in HL18. As discussed above above, in mapping to the physics grid, CAM-SE's Lagrange basis functions are integrated over the *pg*2 control volumes to provide the physics with a volume averaged state. The procedure is accurate to machine precision, conserves thermal energy and dry air mass, and is consistent (i.e., the mapping preserves a constant). The reverse mapping, from the physics grid to the quadrature grid, is done using a tensor-product Lagrange interpolation (see Appendix A
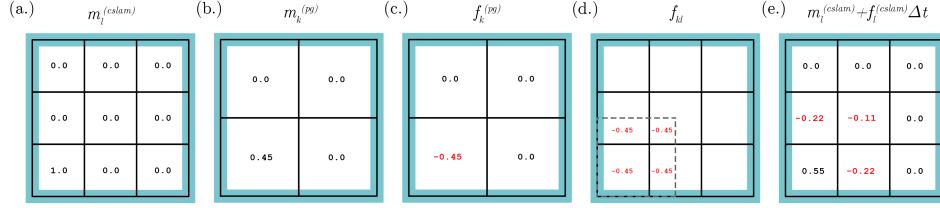
Figure 1. Make captions stand-alone while being concise
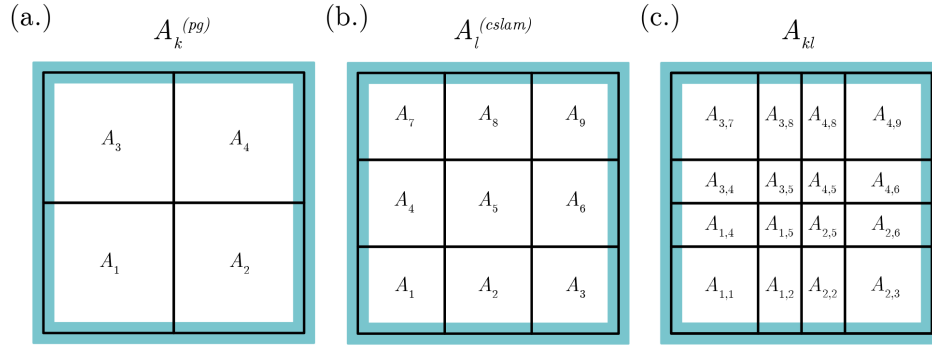
Figure 2. Indice notation for the (a) $pg2$ grid, (b), $pg3$ grid and (c) their exchange grid.

in HL18). The Lagrange interpolation is consistent, conserves dry air mass (Peter, is this true?), but does not conserve thermal energy. Errors arising from the lack of energy conservation were estimated to be small; about two orders of magnitude less than the energy dissipation due to the dynamical core alone.

The semi-Lagrangian advection of tracers in our $pg2$ configuration is solved on the $pg3$ grid (hereafter referred to as the CSLAM grid). Preserving linear correlations in mapping to and from the CSLAM and $pg2$ grids requires additional considerations; one such problem is depicted schematically in Figure 1. Consider a single element of CSLAM control volumes, containing only a single cell with mixing ratio 1.0, and 0.0 everywhere else (m_l; Figure 1a). Assume that the mixing ratios mapped to the $pg2$ grid (m_k; Figure 1b) result in a negative tracer tendency from the physics (f_k; Figure 1c). The non-zero values of the tendencies for $pg2$ areas overlapping CSLAM grid cells originally containing a value of zero ($f_{k,l}$; Figure 1d), are driven negative by the mapped tendency (Figure 1e). Preserving linear correlations is therefore difficult since the mapping between CSLAM and $pg2$ is not reversible. Simulations performed without addressing this artifact were found to be in serious error.

3 Results

A plethora of grids are developed for CAM-SE-CSLAM (Table 1), and used to understand the sensitivity to physics grid resolution, across a wide range of spectral-element grid resolutions. The physics time-step, Δt_{phys}, used for each grid is scaled by the dy-

Table 1. Average equatorial grid spacing, Δx, and model time-step, Δx, used by the physical parameterizations, *phys*, and dynamical core, *dyn*.

Grid name	Δx_{dyn}	Δt_{dyn}	Δx_{phys}	Δt_{phys}
ne20pg3	166.8km	300s	166.8km	1800s
ne30pg2	111.2km	300s	166.8km	1800s
ne30pg3	111.2km	300s	111.2km	1800s

namics time-step to prevent time truncation errors at higher resolutions [*Herrington and Reed*, 2018]. A hierarchy of idealized model configurations are presented (available from CESM2.0; `https://doi.org/10.5065/D67H1H0V`) to illuminate the differences between *pg*2 and *pg*3.

3.1 Moist Baroclinic Wave

Terminator Test of linear-correlation preservation, and tracer mass conservation (just a number showing to within machine precision). Just put it in now, as a reminder for peter to fix the algorithm.

3.2 Held-Suarez with Topography

Flow over rough topography may facilitate significant grid imprinting using the spectral element method [*Lauritzen et al.*, 2015; *Herrington et al.*, in revision]. A Held-Suarez configuration, modified with real world topography is used to identify grid imprinting over mountainous terrain. Figure 3 (middle panel) shows the climatological mean vertical pressure velocity, ω, over the Andes and Himalayan region and at two different levels in the mid-troposphere, using the *ne*30*pg*3 grid. All Held-Suarez simulations are ran for two-years. The figure is displayed as a raster plot on the native physics grid, so that indidual extrema, which characterize the flow over the Andes between about $10° - 20°$ S, may be identified as spurious. Similarly, at the foot of the Himalayas, their are spurious oscillatory bands of upward and downward motion aligned with the element boundaries [see also *Herrington et al.*, in revision].

As discussed in *Herrington et al.* [in revision], grid imprinting over mountainous regions tends to occur in regions of weak stability, and the extrema often manifest as full tropsphere upward/downward couplets. Thus, grid imprinting over mountains may be alleviated through increasing the divergence damping in the model. Figure 3 (right panel) repeats the *ne*30*pg*3 simulation, but increasing the divergence damping coefficient by an order of magnitude. The spurious noise over the Andes and the Himalayas are damped, as grid point extrema tends to be diffused into neighboring grid cells. The wavenumber-power spectrum of the kinetic energy arising from divergent modes is provided in Figure 4, confirming that divergent modes are significantly damped at higher wavenumbers relative to the default *ne*30*pg*3 simulation. Requiring the divergence damping coefficient to be an order of magnitude larger than is required for numerical stability is not ideal from a model development perspective. The hyper-viscosity coefficients are one of the only free-parameters in the dynamical core to tune the kinetic energy spectrum to observations [*Skamarock et al.*, 2014; *Lauritzen et al.*, 2018].

The ω field in a *ne*30*pg*2 simulation is provided in Figure 3 (left panel). Grid cell extrema over the Andes is less prevalent than in the *ne*30*pg*3 simulation, as seen by the reduction in large magnitude ω (e.g., red grid cells). The spurious oscillations at the foot of the Himalayas appears to have been entirely eliminated. This improvement in grid imprinting is due to the consistent sampling of nodal types in the *pg*2 configuration dis-
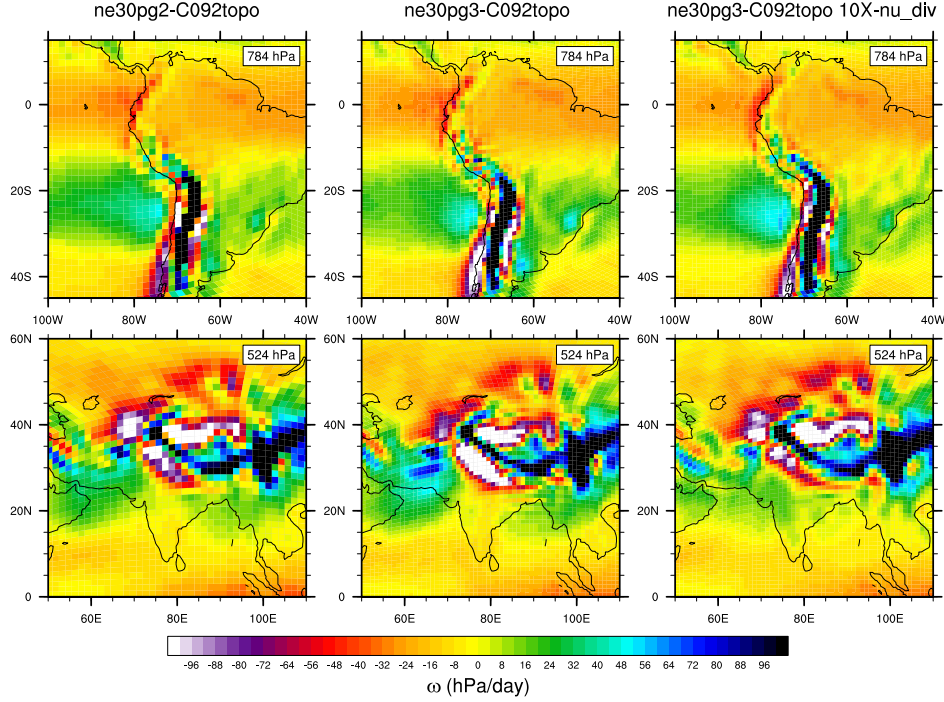
Figure 3. Mean ω at two model levels in the middle troposphere, in a Held-Suarez configuration outfitted with real world topography. (Left) *ne*30*pg*2 (Middle) *ne*30*pg*3 and (Right) *ne*30*pg*3 with the divergence damping coefficient increased by an order of magnitude. The ω fields are computed a two-year simulation. The data are presented on a raster plot in order to identify individual grid cells

cussed in Section **??**. The divergent modes are slightly damped relative to the *ne*30*pg*3 simulations, somewhat sytematically at high wavenumbers, and much less than the simulation using the larger divergence damping coefficient (Figure 4).

3.3 Aqua-planets

The results of the previous section are consistent with our hypothesis, that spurious noise is effectively reduced, and visibly eliminated using a *pg*2 grid. We now turn to the question of whether the coarser resolution physics grid has an impact on the resolved scales of motion. This analysis will make use of an aqua-planet configuration [*Neale and Hoskins*, 2000; *Medeiros et al.*, 2016]; an ocean covered planet in perpetual equinox, and fixed, zonally-symmetric sea surface temperatures idealized after present day Earth. The aqua-planets are run for one simulated year, using CAM, version 6 physics (CAM6; *QPC*6 compset in CESM2.0).

Herrington and Reed [2017] has shown that through assuming the horizontal scale of the Archimedean buoyancy is linearly proportional to the grid spacing, the magnitude of the vertical motion in aqua-planet runs did not scale like the inverse of the grid-spacing across a set of grid resolutions. However, the results of *Herrington and Reed* [2018] indicate that the scaling may be recovered through a more judicous choice of Δt_{phys} (Table 1). To test this idea, three aqua-planet simulations are carried out using the *ne*30*pg*3, *ne*60*pg*3 and *ne*120*pg*3 grids.
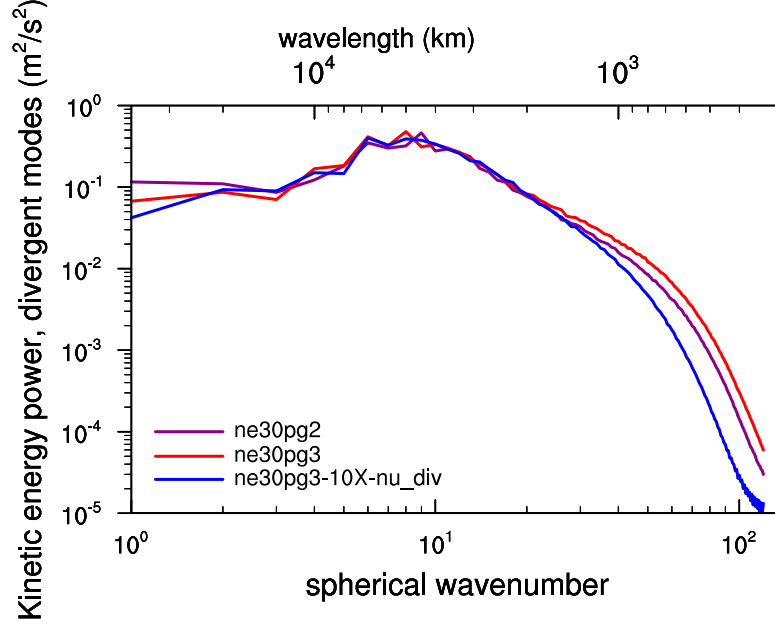
Figure 4. Kinetic energy power spectrum arising from divergent modes in *ne30pg2*, *ne30pg3* and *ne30pg3* with the divergence damping coefficient increased by an order of magnitude ($ne30pg3 - 10X - ne\_div$).

Figure 5a shows the wavenumber-power spectrum of the moist physics temperature tendencies (referred to as *forcing* throughout this study) in the upper troposphere, where statiform heating is common due to detrainment by the deep-convection scheme [*Zhang and McFarlane*, 1995]. There is a clear reduction in forcing scale with resolution, which is consistent with the increased magnitude of ω with resolution, expressed by the probability density distribution (PDF) of upward ω, everywhere in the model (Figure 5b). The PDFs may be scaled to the *ne120pg3* grid using the scaling of *Pauluis and Garner* [2006],

$$P(\omega_s) = \alpha \times P(\omega/\alpha), \tag{12}$$

where $P(\omega_s)$ is the PDF of the scaled ω, ω_s, and α is the ratio of the vertical velocity scale to the vertical velocity scale of the target grid resolution, set to $\alpha = \Delta x_{target}/\Delta x$, after [*Herrington and Reed*, 2018], where Δx is the grid spacing and Δx_{target} is the grid spacing of the target resolution. The scaled PDFs do not line up perfectly on top one another (Figure 5c), but the scaling explains the change in magnitude of ω with resolution to first order. This result is consistent with the notion that the characteristic forcing scales in the simulations are linearly proportional to the grid spacing.

When the physics and dynamics grids are of a different resolution, it is not clear which grid determines the forcing scale. If the characteristic forcing scale is determined by the physics grid spacing, Δx_{phys}, than the *ne30pg2* solution should more closely resemble the *ne20pg3* solution, in which both the physics and dynamics grids are equal to the physics grid of *ne30pg2*. Likewise, if the dynamics grid spacing, Δx_{dyn}, governs the forcing scale than the *ne30pg2* solution would more closely resemble the *ne30pg3* solution. Figure 7a is the PDF of upward ω for simluations using the *ne20pg3*, *ne30pg2* and *ne30pg3* grids. It is clear that the *ne30pg2* solution more closely resembles the *ne30pg3* solution. Scaling the *ne20pg3* solution to *ne30pg3* using eqn. 12 does a fair job of predicting the *ne30pg3* magnitudes (Figure 7b), again consistent with a linear relation between forcing scale and grid spacing. Scaling the *ne30pg2* PDF to the *ne30pg3* grid
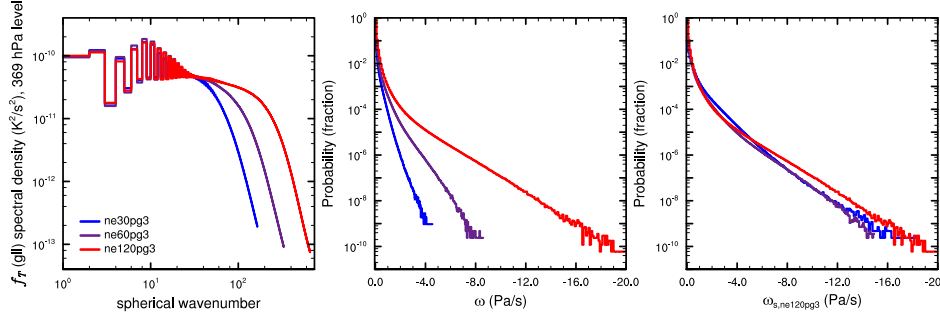
Figure 5. (a) Wavenumber-power spectrum of the temperature tendencies from the moist physics, near the 369 hPa level, (b) probability density distribution and (c) the scaled probability density distribution of upward ω everywhere in the model, from three year long aqua-planet simulations at different grid resolutions. To do: re-do ne120 pdf using binmin of -20 Pa/s.

using Δx_{phys} overestimates the magnitude of ω in the $ne30pg3$ solution, suggesting the characteristic forcing scale can not be proportional to Δx_{phys}.

The dynamical core requires explicit numerical damping to increase with Δx_{dyn} for numerical stability, the exact relation provided in the appendix of *Lauritzen et al.* [2018]. The hyper-viscosity coefficients are therefore smaller (and equal) in the $ne30pg2$ and $ne30pg3$ simulations, relative to the $ne20pg3$ simulation. Figure 7a (green line) shows the PDF of upward ω for a $ne30pg2$ simulation, in which the hyper-viscosity coefficients are increased to $ne20pg3$ values (referred to as $ne30pg2 - hivisc$). The solution now more closely resembles the $ne20pg3$ solution, indicating that an increase in explicit damping results in an increase in characteristic forcing scale. Through scaling the $ne30pg2 - hivisc$ solutions to the $ne30pg3$ grid using Δx_{phys}, the scaled solution lie much closer to the $ne30pg3$ solution, compared wth scaling the default $ne30pg2$ solution using Δx_{phys}. When using a slightly lower resolution physics grid, $\Delta x_{phys}/\Delta x_{dyn} = 1.5$, it seems the forcing scale is determined by Δx_{dyn}, primarily a result of Δx_{dyn} dependent hyper-viscous damping.

The vertical velocity scale is determined by the characteristic forcing scale on the dynamical core grid. Mapping the physics forcing to the dynamics grid using a high-order reconstruction may introduce some fine scale features that the physics grid is unable to support, potentially increasing the vertical velocity scale. A $ne30pg2$ simulation using low-order reconstruction (bilinear interpolation from $pg2$ to GLL, and piecewise-constant mapping between $pg2$ and $CSLAM$ grids; referred to as $ne30pg2 - loworder$) is carried out. The wavenumber-power spectrum of the physics forcing in the upper-troposphere on the physics grid (Figure 8a), and after the forcing is mapped to the dynamics grid (Figure 8b) is provided for the $ne30pg2 - loworder$, $ne30pg2$ and $ne30pg3$ simulations.

On the physics grid, power at high wavenumbers is reduced in $ne30pg2 - loworder$ compared with the default $ne30pg2$ solution, and both have less power than the $ne30pg3$ solution at most wavenumbers. On the dynamics grid, $ne30pg2 - loworder$ is the only solution with a clear reduction in power compared with $ne30pg3$ —the power spectrum of the $ne30pg2$ simulation is indistinguishable from the $ne30pg3$ solution at high wavenumbers (but note the damped oscillations in the $10 - 20$ wavenumber window in $ne30pg2$). The PDFs of upward ω indicate the magnitude of the $ne30pg2$ solution lies intermediate to the two other simulations, but the magnitudes are closer to the $ne30pg3$ solution in the higher probability regions (greater than -2 hPa/day). High-order mapping is therefore

an effective means to mitigate any loss in effective resolution arising from the use of a coarser physics grid.

4 Conclusions

References

Dennis, J. M., J. Edwards, K. J. Evans, O. Guba, P. H. Lauritzen, A. A. Mirin, A. St-Cyr, M. A. Taylor, and P. H. Worley (2012), CAM-SE: A scalable spectral element dynamical core for the Community Atmosphere Model, *Int. J. High. Perform. C.*, *26*(1), 74–89, doi:10.1177/1094342011428142.

Grinstein, F. F., L. G. Margolin, and W. J. Rider (Eds.) (2007), *Implicit Large Eddy Simulation: Computing turbulent fluid dynamics*, Cambridge University Press.

Herrington, A., and K. Reed (2018), An idealized test of the response of the community atmosphere model to near-grid-scale forcing across hydrostatic resolutions, *J. Adv. Model. Earth Syst.*, *10*(2), 560–575.

Herrington, A., P. Lauritzen, M. A. Taylor, S. Goldhaber, B. E. Eaton, J. Bacmeister, K. Reed, and P. Ullrich (in revision), Physics-dynamics coupling with element-based high-order galerkin methods: quasi equal-area physics grid, *Mon. Wea. Rev.*

Herrington, A. R., and K. A. Reed (2017), An explanation for the sensitivity of the mean state of the community atmosphere model to horizontal resolution on aquaplanets, *J. Climate*, *30*(13), 4781–4797, doi:10.1175/jcli-d-16-0069.1.

Jablonowski, C., and D. L. Williamson (2011), The pros and cons of diffusion, filters and fixers in atmospheric general circulation models., in: P.H. Lauritzen, R.D. Nair, C. Jablonowski, M. Taylor (Eds.), Numerical techniques for global atmospheric models, *Lecture Notes in Computational Science and Engineering, Springer, 2010, in press.*, *80*.

Lander, J., and B. Hoskins (1997), Believable scales and parameterizations in a spectral transform model, *Mon. Wea. Rev.*, *125*, 292–303., doi:10.1175/1520-0493.

Lauritzen, P., and J. Thuburn (2012), Evaluating advection/transport schemes using inter-related tracers, scatter plots and numerical mixing diagnostics, *Quart. J. Roy. Met. Soc.*, *138*(665), 906–918, doi:10.1002/qj.986.

Lauritzen, P. H., J. T. Bacmeister, P. F. Callaghan, and M. A. Taylor (2015), Ncar global model topography generation software for unstructured grids, *Geoscientific Model Development Discussions*, *8*(6), 4623–4651, doi:10.5194/gmdd-8-4623-2015.

Lauritzen, P. H., M. A. Taylor, J. Overfelt, P. A. Ullrich, R. D. Nair, S. Goldhaber, and R. Kelly (2017), CAM-SE-CSLAM: Consistent coupling of a conservative semi-lagrangian finite-volume method with spectral element dynamics, *Mon. Wea. Rev.*, *145*(3), 833–855, doi:10.1175/MWR-D-16-0258.1.

Lauritzen, P. H., R. Nair, A. Herrington, P. Callaghan, S. Goldhaber, J. Dennis, J. T. Bacmeister, B. Eaton, C. Zarzycki, M. A. Taylor, A. Gettelman, R. Neale, B. Dobbins, K. Reed, and T. Dubos (2018), NCAR CESM2.0 release of CAM-SE: A reformulation of the spectral-element dynamical core in dry-mass vertical coordinates with comprehensive treatment of condensates and energy, *J. Adv. Model. Earth Syst.*, doi:10.1029/2017MS001257.

Medeiros, B., D. L. Williamson, and J. G. Olson (2016), Reference aquaplanet climate in the community atmosphere model, version 5, *J. Adv. Model. Earth Syst.*, *8*(1), 406–424, doi:10.1002/2015MS000593.

Neale, R. B., and B. J. Hoskins (2000), A standard test for agcms including their physical parametrizations: I: the proposal, *Atmos. Sci. Lett*, *1*(2), 101–107, doi:10.1006/asle.2000.0022.

Neale, R. B., C.-C. Chen, A. Gettelman, P. H. Lauritzen, S. Park, D. L. Williamson, A. J. Conley, R. Garcia, D. Kinnison, J.-F. Lamarque, D. Marsh, M. Mills, A. K. Smith, S. Tilmes, F. Vitt, P. Cameron-Smith, W. D. Collins, M. J. Iacono, R. C. Easter, S. J. Ghan, X. Liu, P. J. Rasch, and M. A. Taylor (2012), Description of the NCAR Commu-

nity Atmosphere Model (CAM 5.0), *NCAR Technical Note NCAR/TN-486+STR*, National Center of Atmospheric Research.

Pauluis, O., and S. Garner (2006), Sensitivity of radiative–convective equilibrium simulations to horizontal resolution, *J. Atmos. Sci.*, *63*(7), 1910–1923.

Randall, D., M. Khairoutdinov, A. Arakawa, and W. Grabowski (2003), Breaking the cloud parameterization deadlock, *Bulletin of the American Meteorological Society*, *84*(11), 1547–1564.

Shutts, G. (2005), A kinetic energy backscatter algorithm for use in ensemble prediction systems, *Quart. J. Roy. Meteorol. Soc.*, *131*, 3079–3102.

Skamarock, W. (2011), Kinetic energy spectra and model filters, in: P.H. Lauritzen, R.D. Nair, C. Jablonowski, M. Taylor (Eds.), Numerical techniques for global atmospheric models, *Lecture Notes in Computational Science and Engineering, Springer*, *80*.

Skamarock, W. C., S.-H. Park, J. B. Klemp, and C. Snyder (2014), Atmospheric kinetic energy spectra from global high-resolution nonhydrostatic simulations, *Journal of the Atmospheric Sciences*, *71*(11), 4369–4381, doi:10.1175/JAS-D-14-0114.1.

Taylor, M., J. Edwards, and A. St-Cyr (2008), Petascale atmospheric models for the community climate system model: new developments and evaluation of scalable dynamical cores, *J. Phys.: Conf. Ser.*, *125*, doi:10.1088/1742-6596/125/1/012023.

Wedi, N. P. (2014), Increasing horizontal resolution in numerical weather prediction and climate simulations: illusion or panacea?, *Philosophical Transactions of the Royal Society of London A: Mathematical, Physical and Engineering Sciences*, *372*(2018), doi:10.1098/rsta.2013.0289.

Williamson, D. L. (1999), Convergence of atmospheric simulations with increasing horizontal resolution and fixed forcing scales, *Tellus A*, *51*, 663–673, doi:10.1034/j.1600-0870.1999.00009.x.

Zhang, G., and N. McFarlane (1995), Sensitivity of climate simulations to the parameterization of cumulus convection in the canadian climate center general-circulation model, *ATMOSPHERE-OCEAN*, *33*(3), 407–446.
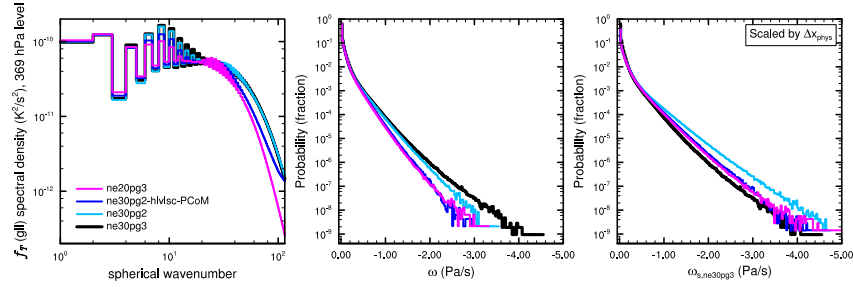
Figure 6. (Left) Wavenumber-power spectrum of the temperature tendencies from the moist physics, near the 369 hPa level, (Middle) probability density distribution and (Right) the scaled probability density distribution of upward ω everywhere in the model. To do: make legend and re-do 0.25 degree sims using binmin of -20 Pa/s.
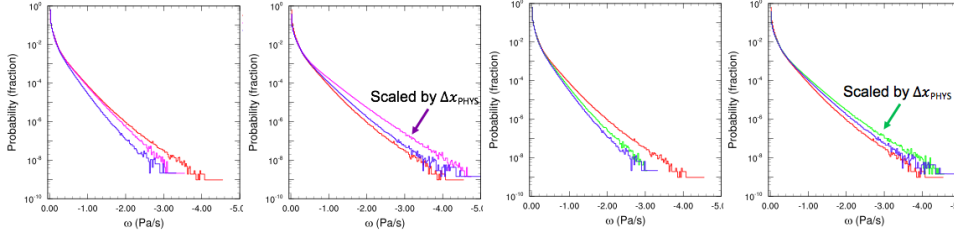
Figure 7. (a) Probability density distribution and (b) the scaled probability density distribution of upward ω everywhere in the model, from four different year long aqua-planet simulations at different grid resolutions. To do: make this a two panel plot with a clear legend.
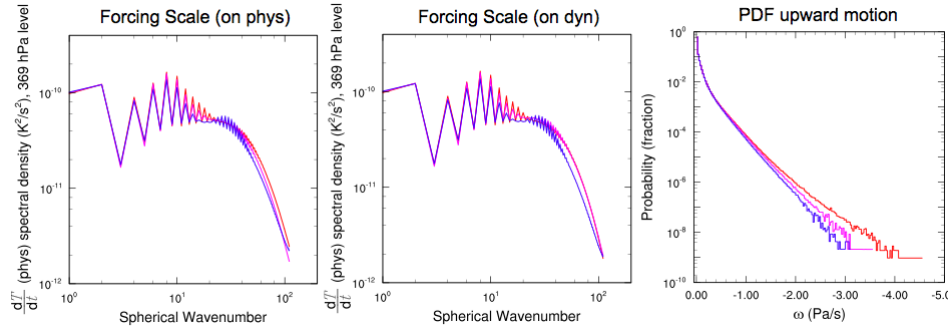

Figure 8. (a) Wavenumber-power spectrum of the temperature tendencies from the moist physics, near the 369 hPa level, on (a) the physics grid, and (b) the dynamics grid, and (c) the probability density distribution of upward ω everywhere in the model To do: make a clear legend.